Nanoscale

Fusion growth patterns in atomically precise metal nanoclusters

Journal:	*Nanoscale*
Manuscript ID	NR-MRV-07-2019-005789.R1
Article Type:	Minireview
Date Submitted by the Author:	12-Aug-2019
Complete List of Authors:	Du, Xiangsha; Carnegie Mellon University, Chemistry Chai, Jinsong; Anhui University Yang, Sha; anhui university, Li, Yingwei; Carnegie Mellon University, Chemistry Higaki, Tatsuya; Carnegie Mellon University, Chemistry; The University of Tokyo, Li, Site; Carnegie Mellon University, Chemistry Jin, Rongchao; Carnegie Mellon University, Chemistry

Nanoscale

Fusion growth patterns in atomically precise metal nanoclusters

Received 00th January 20xx,
Accepted 00th January 20xx

DOI: 10.1039/x0xx00000x

Xiangsha Du,[a] Jinsong Chai,[a] Sha Yang,[a] Yingwei Li,[a] Tatsuya Higaki,[a] Site Li,[a] and Rongchao Jin[a]*

Atomically precise nanoclusters of coinage metals in the 1-3 nm size regime are being intensively pursued in recent years. Such nanoclusters are attractive as they fill in the gap between small molecules (< 1 nm) and regular nanoparticles (> 3 nm). This intermediate identity endows nanoclusters with unique physicochemical properties and provides nanochemists opportunities to understand the fundamental science of nanomaterials. Metal nanoparticles are well known to exhibit plasmon resonances upon interaction with light; however, when the particle size is downscaled to the nanocluster regime, the plasmons fade out and step-like absorption spectra characteristic of cluster sizes are manifested due to strong quantum confinement effects. Recent research has revealed that nanoclusters are commonly composed of a distinctive kernel and a surface-protecting shell (or staple-like metal-ligand motifs). Understanding the kernel configuration and evolution is one of the central topics in nanoscience research. This Review summarizes the recent progress in identifying the growth patterns of atomically precise coinage nanoclusters. Several basic kernel units have been observed, such as the M_4, M_{13} and M_{14} polyhedrons (where, M = metal atom). Among them, the tetrahedral M_4 and icosahedral M_{13} units are the most common ones, which are adopted as building blocks to construct larger kernel structures via various fusion or aggregation modes, including the vertex- and face-sharing mode, the double-strand and alternate single-strand growth, and cyclic fusion of M_4 units, as well as the fcc-based cubic growth pattern. The identification of the kernel growth pathways has led to deeper understanding of the evolution of electronic structure and optic properties.

1. Introduction

Controlling nanoparticles with atomic precision has long been the major dream of nanochemists, because achieving atomically precise nanoparticles (called nanoclusters) is a prerequisite to unveiling the total structures of nanoparticles (in particular the surface structures).[1-5] Achieving the atomic-level structures of nanoclusters is of paramount importance for understanding their stability, interfacial bonding, and the physicochemical properties.[6-10] While synthetic control at the atomic level is already routine in molecular chemistry, the same goal is still very challenging in nanochemistry, as the latter is much more complex than the former. Nevertheless, intense research in the past years has established some successful methods, such as the size-focusing and LEIST (abbreviation for ligand-exchange-induced size/structure transformation) synthetic methodologies,[11,12] which paved the way to rational synthesis of atomically precise metal nanoclusters with molecular purity. Crystallization of such high-quality nanoclusters has enabled the total structure (kernel and surface) determination by X-ray crystallography. With the solved total structures, not only the kernels (i.e., the arrangements of metal atoms) but also the surface structures (i.e., the arrangements of ligands and the bonding between the ligands and the metal core) have been understood; many other fundamental issues, such as the ligand-core coordination pattern, structure-property relationship, size dependence, shape control, are also partially understood.

Recent research in structure determination of metal nanoclusters has demonstrated that the kernel can be single crystalline (e.g., face-centered cubic (fcc),[13] body-centered cubic (bcc),[14] hexagonal close-packed (hcp)[15,16]) or multiply twined (e.g., icosahedron,[17,18] decahedron[19]) structures. The observed polyhedron-based kernels, such as the M_4 tetrahedron, M_7 decahedron, and M_{13} icosahedron with high symmetry, are one of the primary factors that are responsible for the high stability of nanoclusters.

Owing to the high surface-to-volume ratio in nanoclusters, the surface structure also plays a crucial role in the stability, reactivity, and physicochemical properties. Taking gold as an example, the determined structures have unveiled that the surfaces of $Au_n(SR)_m$ nanoclusters are mainly protected by $Au_x(SR)_{x+1}$ staple-like motifs such as monomer $Au(SR)_2$, dimer $Au_2(SR)_3$, trimmer $Au_3(SR)_4$, tetramer $Au_4(SR)_5$ and the pentamer $Au_5(SR)_6$.[11-23] In such staple motifs, the Au(I) atoms

[a] Department of Chemistry, Carnegie Mellon University, Pittsburgh, PA 15213, USA.
* Correspondence: (R.J.) Email: rongchao@andrew.cmu.edu

are bonded to two -SR groups in a linear fashion (i.e., the S-Au-S angle being ~180°), and the S atom of the terminal -SR group is further bonded to a kernel Au atom, with the Au-S-Au angle ranging from ~75° to 108°. Smaller nanoclusters typically have more curved surfaces and thus require longer staple motifs for protection, whereas in larger spherical nanoclusters, shorter staple motifs are found to be predominant in the surface structure.[19]

Based on the reported metal nanocluster structures, one remarkable structural characteristic can be identified, that is, quite many structures can be considered as being built from basic kernel units such as M_4, M_6, M_7 and M_{13} polyhedrons. A few growth modes, including fusion, interpenetration, shell-by-shell, layer-by-layer and vertex-sharing are observed for the formation of larger structures from the basic units.[19,24,25] We shall refer these clusters as "superclusters" or "cluster of clusters". Moreover, the structures of metal nanoclusters resemble the packing of atoms into molecules.[19]

In terms of properties, the optical properties of gold nanoparticles have long been fascinating since Faraday's time. Different from the surface plasmon resonance (SPR) in conventional metal nanoparticles, nanoclusters smaller than $Au_{279}(SR)_{84}$ (2.2 nm metal core) possess discrete energy levels due to quantum confinement effect and thus exhibit step-like multiband absorption spectra.[26,27] Recently, a sharp transition from non-metallic $Au_{246}(SR)_{80}$ to plasmonic $Au_{279}(SR)_{84}$ has been revealed.[26] The unique properties of metal nanoclusters endow them with great potential for applications in catalysis, bioimaging, chemical sensing, and so on. Since the structures of nanoclusters exhibit certain patterns,[19] it is highly desirable to explore the structure-property correlation and thus understand the size evolution.

In this Review, we discuss a fusion growth mode identified in several series of nanoclusters based on different polyhedral building blocks. The different stacking modes include the icosahedral M_{13}-based linear and cyclic growth patterns, the double helical growth of tetrahedral Au_4 units, and the fcc-unit-based size evolution via either face- or vertex-sharing. The relevant evolution of the optical properties of such nanoclusters is also discussed.

2. Fusion of icosahedral building blocks

2.1 Linear fusion of Au_{13} units to Au_{25} and Au_{37} via vertex-sharing

The 13-atom icosahedral structure (M_{13}) is a ubiquitous structural unit, which is composed of a centre and a 12-atom shell of icosahedral geometry (Figure 1a). Such a M_{13} kernel was reported in many works, e.g. the $[Au_{13}(dppe)_5Cl_2]^{3+}$ cluster (where, dppe = 1,2-bis(diphenylphosphino) ethane).[28] A rod-like bi-icosahedral $[Au_{25}(PPh_3)_{10}(SR)_5Cl_2]^{2+}$ nanocluster (R=C_2H_5 or C_2H_4Ph) has also been successfully synthesized and characterized.[29,30] The Au_{25} kernel structure is constructed via vertex-sharing of two Au_{13} units (i.e., 13 + 13 - 1 = 25). More interestingly, another icosahedron-based structure has recently been unveiled, with its formula being $[Au_{37}(PPh_3)_{10}(SR)_{10}Cl_2]^+$ (where R = C_2H_4Ph), in which the core comprises three Au_{13} building blocks that are linearly assembled together via vertex-sharing.[31]

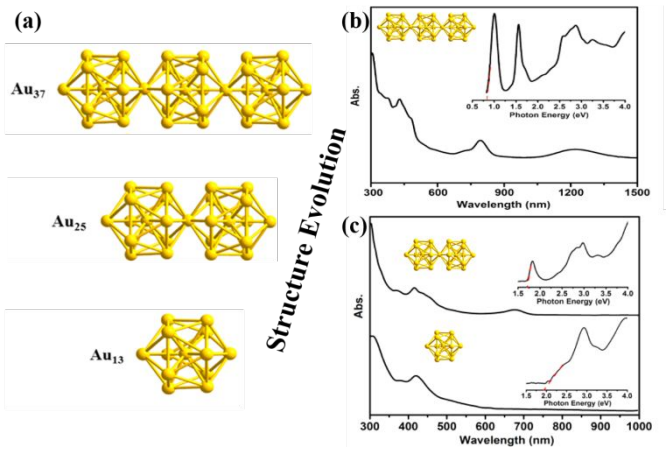

Figure 1. Kernel evolution in the Au_{13}-Au_{25}-Au_{37} series (a); UV-vis-NIR spectra of the Au_{37} (b) and Au_{25} and Au_{13} (c) nanoclusters (insets: spectra on the photon energy scale). Adapted with permission from ref 31, copyright © 2015 American Chemical Society.

The optical absorption spectra of $[Au_{13}(dppe)_5Cl_2]^{3+}$, $[Au_{25}(PPh_3)_{10}(SR)_5Cl_2]^{2+}$, and $[Au_{37}(PPh_3)_{10}(SR)_{10}Cl_2]^+$ (Figure 1b, 1c) illustrate a uniform evolution of the optical properties in this series with increasing number of Au_{13} units. The Au_{13} shows superatomic $1S^21P^6$ electronic structure evolved from Au(6s6p).[32] As shown in the absorption spectra, the peaks below 500 nm are relevant to the electronic transitions within individual icosahedral Au_{13} units and these are preserved in larger sizes. On the other hand, upon assembly of two or more icosahedra, new collective features also emerge, such as the long wavelength bands, which are HOMO-LUMO peaks and redshift from ~500 nm (for the Au_{13} cluster) to 670 nm (for Au_{25}) to 1230 nm (for Au_{37}).[32] The increasing size is accompanied by decreasing energy gap from Au_{13} 1.96 eV to Au_{25} 1.73 eV to Au_{37} 0.83 eV. The Au_{37} also exhibits intriguing electron localization upon photoexcitation.[33]

Of note, Au/Ag alloy nanoclusters with linearly-assembled icosahedra as kernels were earlier reported by Teo' group, such as $[(Ph_3P)_{12}Au_{13}Ag_{12}Cl_6]^{m+}$, which comprised a vertex-sharing biicosahedral $Au_{13}Ag_{12}$.[34] Recently, Zhu's group also reported vertex-sharing biicosahedral $Cu_xAu_{25-x}(PPh_3)_{10}(PhC_2H_4S)_5Cl_2^{2+}$ and $[Ag_xAu_{25-x}(PPh_3)_{10}(SC_2H_4Ph)_5Cl_2]^{2+}$ nanoclusters.[35,36] In theoretical work, Iwasa et al discussed a M_{25} constructed from $PtAu_{12}$ and $HgAu_{12}$ units and found that the HOMO and LUMO are well localized to the $PtAu_{12}$ and $HgAu_{12}$ units, respectively, forming a heterojunction with charge transfer from $PtAu_{12}$ to $HgAu_{12}$ upon visible light excitation and hence a large dipole moment.[37]

2.2 Cyclic fusion of Au_{13} units to $Au_{37/38}$ and Au_{60} via vertex-sharing

Superclusters can be constructed from the basic units not only by linear fusion, but also by a cyclic mode. For example, Teo et al. earlier reported two Au/Ag alloy nanoclusters of 37 and 38 atoms (Figure 2).[25,38] The 37-atom [(p-$Tol_3P)_{12}Au_{18}Ag_{19}Br_{11}$]($AsF_6$) and 38-atom [(p-$Tol_3P)_{12}Au_{18}Ag_{20}Cl_{14}$] nanoclusters are both composed of triicosahedra via sharing three vertices in a cyclic manner, plus one or two capping atoms above/below the central triangular face. Zhu et al recently reported another alloy nanocluster, formulated as $Cu_3Au_{34}(PPh_3)_{13}(^tBuPhCH_2S)_6S_2^{3+}$, which also possesses a cyclic triicosahedral M_{36} kernel.[35]

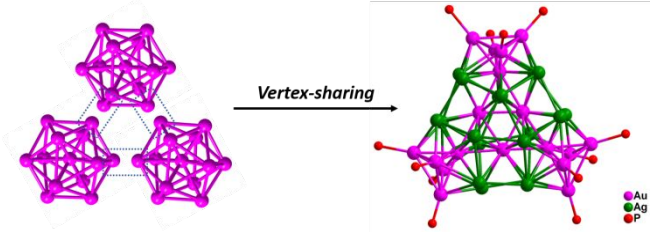

Figure 2. M_{36} framework of Au/Ag alloy superclusters [(p-$Tol_3P)_{12}Au_{18}Ag_{19}Br_{11}$]($AsF_6$) and [(p-$Tol_3P)_{12}Au_{18}Ag_{20}Cl_{14}$]. Redrawn from ref 38.

Assembly of five icosahedral Au_{13} building blocks has recently been observed in a Au_{60} nanocluster ($13 \times 5 - 5 = 60$) co-protected by selenolate and phosphine ligands (Figure 3).[39] Its formula was determined to be [$Au_{60}Se_2(Ph_3P)_{10}(SePh)_{15}$]($SbF_6$). X-ray crystallography analysis shows that the Au_{60} kernel contains five icosahedral Au_{13} units and every two adjacent units share a vertex atom in a cyclic fashion, with the entire structure clipped together by five Au-Se-Au linkages in a circle. Due to the linking of five Au_{13} units, both the HOMO and LUMO electronic states are changed. The HOMO–LUMO peak shifts from ~500 nm (for Au_{13}) to 835 nm (for Au_{60}). The absorption peak at 835 nm is assigned to a new electronic transition because of the pentameric structure.

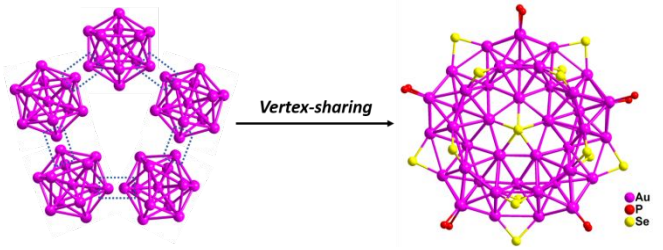

Figure 3. Vertex-sharing of five icosahedra into $[Au_{60}Se_2(PPh_3)_{10}(SePh)_{15}]^+$. Redrawn from ref 39.

2.3 Linear growth via face-sharing

The fusion of icosahedra can also be implemented through face-sharing as in the case of $Au_{38}(SC_2H_4Ph)_{24}$.[40] This cluster has a face-fused biicosahedral Au_{23} kernel ($13 \times 2 - 3 = 23$) via sharing a common Au_3 face of the two units (Figure 4a). The kernel is protected by three monomeric staples (RS-Au-SR) at the waist and six dimeric staples (RS-Au-S(R)-Au-SR) at the top and bottom icosahedra. The rotary arrangement of the dimeric staples gives rise to chirality of the cluster, albeit the Au_{23} kernel is achiral.

Interestingly, Maran's recent work revealed an aggregative transformation of the stable $Au_{25}(SR)_{18}$ cluster into $Au_{38}(SR)_{24}$ without any co-reagent, which offered insights into the bottom-up assembly of the fundamental Au_{13} units into superstructures in solution.[41] As shown in Figure 4b, after dissolving the Au_{25} in toluene at 65 °C, the original UV-Vis spectrum of $Au_{25}(SR)_{18}$ (black curve) undergoes progressive changes, which are particularly evident in the 500 to 800 nm region, and 10-14 days later, the purified product showed a spectrum virtually identical to that of the $Au_{38}(SC_2H_4Ph)_{24}$, indicating a thermal conversion of mono-icosahedral Au_{25} to biicosahedral Au_{38} via fusion growth.

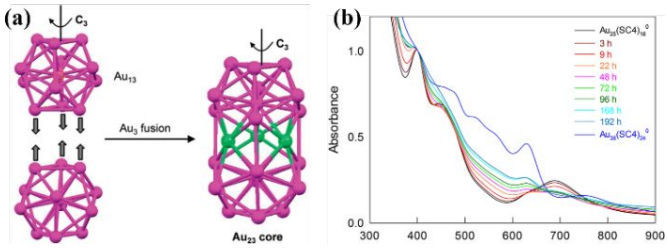

Figure 4. (a) Face-fused biicosahedral Au_{23} kernel. (b) Conversion of $Au_{25}(SR)_{18}$ to $Au_{38}(SR)_{24}$ monitored by UV–vis spectroscopy for the reaction of 30 mM $Au_{25}(SC_4)_{18}^0$ at 65 °C in toluene. Panel a: Adapted with permission from ref 20, Copyright © 2016, American Chemical Society; panel b: Adapted with permission from ref 41, Copyright © 2018, American Chemical Society.

Face-fused biicosahedral (Pd_{23}) and triicosahedral (Pd_{33}) kernels were also previously found in the phosphine/carbonyl-protected $Pd_{39}(CO)_{23}(PMe_3)_{16}$ and $Pd_{69}(CO)_{36}(PEt_3)_{18}$, respectively.[6]

2.4 Linear growth via edge-sharing

In addition to the afore-discussed linear extension of Au_{13} units via vertex- and face-sharing, which have been experimentally identified, the edge-sharing mode may also be possible. Häkkinen et al. theoretically investigated a series of linear superclusters, including $Au_{40}(SH)_{24}$, $Au_{57}(SH)_{32}^-$, $Au_{74}(SH)_{40}$ and $Au_{108}(SH)_{56}$ that are built out of 2, 3, 4, and 6 icosahedral Au_{13} units, respectively (Figure 5).[42,43] In these structures, the assembly of icosahedra is arranged in an edge-to-edge manner with 90° rotation to each other. Similar to the structure proposed for $Au_{40}(SR)_{24}$, each waist of the two Au_{13} units is protected by four RS-Au-SR units, and both ends of the resulted supercluster are capped by two RS-Au-SR-Au-SR motifs and one RS-Au-SR motif.

Using the model set for the above series, they further predicted the structure of a previously reported 11 kDa[44-46] species to be $Au_{54}(SR)_{30}$ in the form of [Au_{36}@(RS-Au-SR)$_6$(RS-Au-SR-Au-SR)$_6$], in which the Au_{36} kernel is predicted to be a heterodimer of Au_{13} (the kernel of $Au_{25}(SR)_{18}$) and Au_{23} (the face-fused biicosahedral kernel of $Au_{38}(SR)_{24}$) via edge-contact (Figure 5, the bottom right inset). The surface-protecting staple motifs are arranged in a manner reminiscent of the structure of $Au_{38}(SR)_{24}$. The optical absorption spectrum,

including the number of peaks, energy positions (within 0.1 eV) and relative intensities of the characteristic features of the calculated $Au_{54}(SH)_{30}$ agree well with that of the synthesized 11 kDa species.

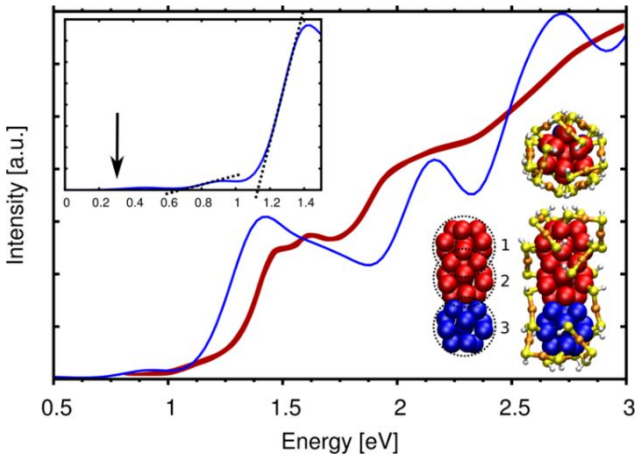

Figure 5. Calculated absorption spectrum (blue curve) for the model cluster $Au_{54}(SH)_{30}$, compared to the experimental data (red curve); insets: photon-energy scale spectra and the kernel structure as a heterodimer fused from the Au_{13} kernel of $Au_{25}(SR)_{18}$ (blue) and the Au_{23} kernel of $Au_{38}(SR)_{24}$ (red). Adapted with permission from ref 42, Copyright © 2014, American Chemical Society.

3. Fusion of Au_4 tetrahedral building blocks

3.1 Double-stranded growth

Zeng et al. revealed an intriguing kernel evolution pattern in a series of 4-tert-butylbenzenethiolate (TBBT)-protected gold nanoclusters, namely, a double-stranded growth.[47,48] The series has a common formula, $Au_{8n+4}(TBBT)_{4n+8}$ with *n* ranging from 2 to 6, which gives $Au_{20}(TBBT)_{16}$, $Au_{28}(TBBT)_{20}$, $Au_{36}(TBBT)_{24}$, $Au_{44}(TBBT)_{28}$ and $Au_{52}(TBBT)_{32}$.[47-50] Gold atoms in these clusters can be divided into a kernel and staple motifs of the form $Au_x(SR)_{x+1}$ (Figure 6). The $Au_{20}(TBBT)_{16}$ has a bitetrahedral Au_7 kernel which is formed by vertex-sharing of two tetrahedra. Compared with Au_{20}, the kernel of $Au_{28}(TBBT)_{20}$ consists of one more such Au_7 unit, and the two Au_7 units are arranged in a double-helix pattern. Then, after successively adding two tetrahedra to the bottom of the double helix, n tetrahedra are observed in the kernels of the magic series, that is, from 2 tetrahedra in $Au_{20}(TBBT)_{16}$ to 4 tetrahedra in $Au_{28}(TBBT)_{20}$, 6 tetrahedra in $Au_{36}(TBBT)_{24}$, 8 tetrahedra in $Au_{44}(TBBT)_{28}$, and 10 tetrahedra in $Au_{52}(TBBT)_{32}$.

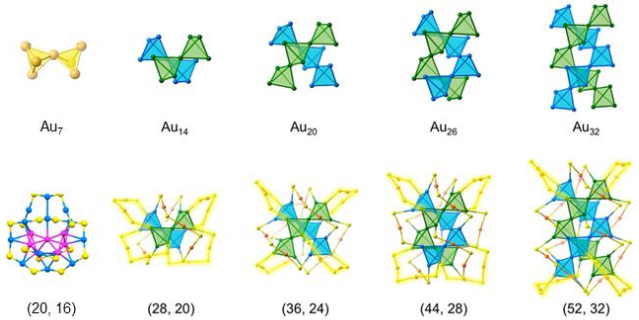

Figure 6. Growth pattern in the $Au_{8n+4}(SR)_{4n+8}$ magic series, n = 2–6. Adapted with permission from ref 47 & 48, Copyright © 2014 & 2016, American Chemical Society.

In theoretical work, Pei et al[51, 52] discussed a unified view of the double helical Au_4-tetrahedron chain structure, electronic structure, magic stability and size-dependent optical absorption properties of this series. Gao and Zeng identified that the local stability of each tetrahedral Au_4 unit contributes to the overall cluster stability.[53] An interesting oscillating dependence of transformation energy on the n was found,[51] with the odd-n nanoclusters showing more favourable (negative) reaction energies than the even-n nanoclusters in the series.

As for the surface structure, Au_{20} has three staple motifs (including one $Au_3(SR)_4$ trimer and two $Au(SR)_2$ monomers) protecting the bitetrahedral Au_7 kernel, and the remaining eight Au atoms and eight -SR form a ring structure to wrap the kernel. The other sizes in the series have common $Au_2(SR)_3$ dimeric staple motifs protecting at the two ends of the double helixes, whereas the waists are protected by different staples depending on the length of double helixes, with $Au_3(SR)_4$ trimer for Au_{28}, dimers for Au_{36}, and dimers plus $Au(SR)_2$ monomers for Au_{44} and Au_{52}. The free valence electron count for the series increases from 4e, 8e, 12e, 16e, to 20e, which matches well with the number of tetrahedral units in the corresponding nanocluster, with each tetrahedral unit requiring two electrons for stabilization.

The identical kernel units and the same protecting thiolate (TBBT) provide a great opportunity to investigate the property evolution in such a magic-series of nanoclusters. The optical absorption spectra (Figure 7) of the $Au_{8n+4}(TBBT)_{4n+8}$ (n = 3 − 6) nanoclusters exhibit similar profiles, with the high energy absorption peak centered at ~400 nm and a plateau in the longer wavelength region. DFT calculations revealed that the ~400 nm peak is attributed to the *d* to *sp* transition and is less sensitive to size evolution than the long-wavelength peak; the latter arises from *sp* to *sp* transition in the kernel, since *d* electrons are less delocalized than the *sp* electrons. Thus, as the size increases from Au_{28}, Au_{36}, Au_{44}, to Au_{52}, the high energy peak slightly redshifts from 366, 376, 380, to 396 nm, and the onset of absorbance (e.g., optical gap) exhibits more redshifts, i.e., from 702, 704, 820, to 890 nm (E_g = 1.77, 1.76, 1.51, 1.39 eV, respectively). Sizes larger than $Au_{52}(TBBT)_{32}$ have also been predicted[53,54] and deserve future efforts of experimental synthesis.

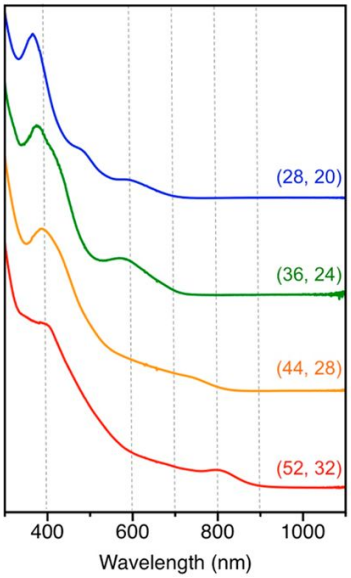

Figure 7. Size-dependent UV–vis spectra. Adapted with permission from ref 47, Copyright © 2016, American Chemical Society.

3.2 Alternate single-stranded evolution at both ends

Another series of nanoclusters are surface protected by cyclohexanethiolate (S-c-C_6H_{12}). Similar to the series of Au_{20}, Au_{28}, Au_{36}, Au_{44}, and Au_{52}, nanoclusters of Au_{28}(S-c-C_6H_{11})$_{20}$, Au_{34}(S-c-C_6H_{11})$_{22}$ and Au_{42}(S-c-C_6H_{11})$_{26}$ were also found to adopt the Au_4 tetrahedron as the building block, but the kernel growth pattern is quite different.[55,56] Distinguished from the former series of adding Au_4 tetrahedra to the bottom of the double helixes, the latter series grows by tetrahedron addition to both ends of one helix; that is, from Au_{28}(S-c-C_6H_{11})$_{20}$ to Au_{34}(S-c-C_6H_{11})$_{22}$, two Au_4 units are added to the two ends of one helix (one Au_4 for each end, Figure 8A/B), from Au_{34}(S-c-C_6H_{11})$_{22}$ to Au_{42}(S-c-C_6H_{11})$_{26}$, another two Au_4 are added to the two ends of the other helix (Figure 8C). This growth pattern results in 4 tetrahedra in Au_{28}(S-c-C_6H_{11})$_{20}$, 6 tetrahedra in Au_{34}(S-c-C_6H_{11})$_{22}$ and 8 tetrahedra in Au_{42}(S-c-C_6H_{11})$_{26}$. Although Au_{34}(S-c-C_6H_{11})$_{22}$ and Au_{36}(TBBT)$_{24}$, Au_{42}(S-c-C_6H_{11})$_{26}$ and Au_{44}(TBBT)$_{28}$ have the same counts of tetrahedra in their kernels, their difference in the Au/S ratio and structure are generated from the distinguished protecting ligands (PET vs. S-c-C_6H_{12}). Moreover, the disparity of ligands results in different staple motifs even in the same Au/S ratio (i.e., the pair of Au_{28}(S-c-C_6H_{11})$_{20}$ and Au_{28}(TBBT)$_{20}$), that is, the cyclohexanethiolate-protected Au_{28}(S-c-C_6H_{11})$_{20}$ is capped by two trimeric staples and two monomeric staples, while in Au_{28}(TBBT)$_{20}$ four $Au_2(SR)_3$ staple motifs are observed. The bi-tetrahedron chain in Au_{34}(S-c-C_6H_{11})$_{22}$ is protected by three $Au_3(SR)_4$ trimeric staples, whereas the other chain is protected by five $Au(SR)_2$ monomers. For the Au_{42}(S-c-C_6H_{11})$_{26}$, the double helixes are protected by six $Au_2(SR)_3$ dimers at the top and bottom and four $Au(SR)_2$ monomers at the waist.

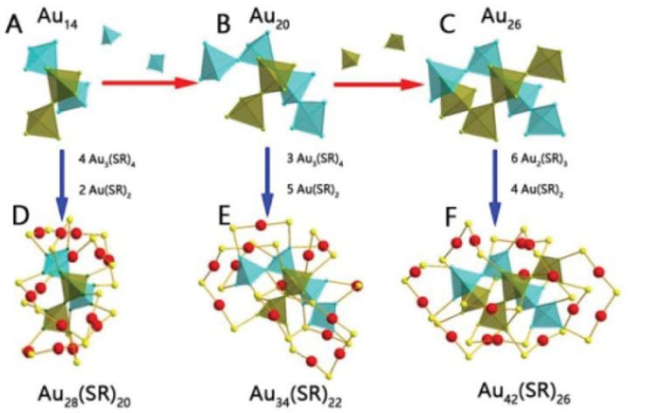

Figure 8. The kernel and total structure of Au_{28}(S-c-C_6H_{11})$_{20}$, Au_{34}(S-c-C_6H_{11})$_{22}$ and Au_{42}(S-c-C_6H_{11})$_{26}$: Au_{14} kernel of Au_{28}(S-c-C_6H_{11})$_{20}$ (A); Au_{20} kernel of Au_{34}(S-c-C_6H_{11})$_{22}$ (B); Au_{26} kernel of Au_{42}(S-c-C_6H_{11})$_{26}$ (C); Au_{28}(S-c-C_6H_{11})$_{20}$ framework (D); Au_{34}(S-c-C_6H_{11})$_{22}$ framework (E); and Au_{42}(S-c-C_6H_{11})$_{26}$ framework (F). Adapted with permission from ref 56, Copyright © 2017, Royal Society of Chemistry.

Electrochemical measurements of the Au_{28}(S-c-C_6H_{11})$_{20}$, Au_{34}(S-c-C_6H_{11})$_{22}$ and Au_{42}(S-c-C_6H_{11})$_{26}$ nanoclusters (in 0.1 M Bu_4NPF_6–CH_2Cl_2) determined their electrochemical gaps to be 2.04, 1.91 and 1.62 V, respectively. After subtracting the charging energy (~0.29 V), the E_g values are in good accordance with the optical gaps (1.77, 1.68, and 1.40 eV, respectively). As expected, the E_g value decreases as the size increases.

3.3 Cyclic growth

Unlike the one-dimensional growth in the double-helix tetrahedron chains in Au_{28}, Au_{36}, Au_{44}, and Au_{52}, Pei and Zhu et al. reported a new tetrahedron-based cyclic evolution series.[57,58] The series contains four sizes, namely, $Au_{22}(SR)_{18}$ (R = methyl), $Au_{28}(SR)_{20}$ (R = methyl), Au_{34}(S-c-C_6H_{11})$_{22}$ and Au_{40}(o-MBT)$_{24}$ (o-MBT = 2-methylbenzenethiol).[52,56,59,60] The optimal structures of $Au_{22}(SR)_{18}$ and $Au_{28}(SR)_{20}$ are theoretically predicted by DFT calculations. The four nanoclusters belong to a uniform $Au_{16+6N}(SR)_{16+2N}$ series (N = 1–4). In each step of the cluster size evolution, a $Au(SR)_2$ unit in the $[Au_6(SR)_6]$ complex is consumed, and a bitetrahedral Au_7 unit is formed (Figure 9). The structure model of $Au_{22}(SR)_{18}$ contains a bitetrahedral Au_7 kernel protected by a $[Au_6(SR)_6]$ ring and three $Au_3(SR)_4$ staple motifs. The predicted $Au_{28}(SR)_{20}$ has two bitetrahedral Au_7 units protected by two monomers and four trimers, so it has the same kernel as the two known Au_{28} nanoclusters with experimentally determined structures (i.e., Au_{28}(S-c-C_6H_{11})$_{24}$ and Au_{28}(TBBT)$_{24}$)[49,55] but with different staple motifs on the surface of the third $Au_{28}(SR)_{20}$ structure (Figure 9, red box). The Au_{34}(S-c-C_6H_{11})$_{22}$ contains three linearly assembled bitetrahedra, also observed in the structure are three trimeric staples as well as five monomers. The further evolution of one more bitetrahedron makes the tetrahedral units coiled up into a Kekulé-like superstructure of $Au_{40}(SR)_{24}$. The Kekulé ring is protected by six monomeric $Au(SR)_2$ staples, while the central Au_7 is capped by three trimers. The free electron counts of the clusters obey the same rule as in the Au_{20} to Au_{52} series or the Au_{28} to Au_{42} series, i.e., each tetrahedron contains 2e. Thus, $Au_{22}(SR)_{18}$, $Au_{28}(SR)_{20}$, Au_{34}(S-c-C_6H_{11})$_{22}$ and Au_{40}(o-MBT)$_{24}$ have 4, 8, 12, and 16 e, respectively.

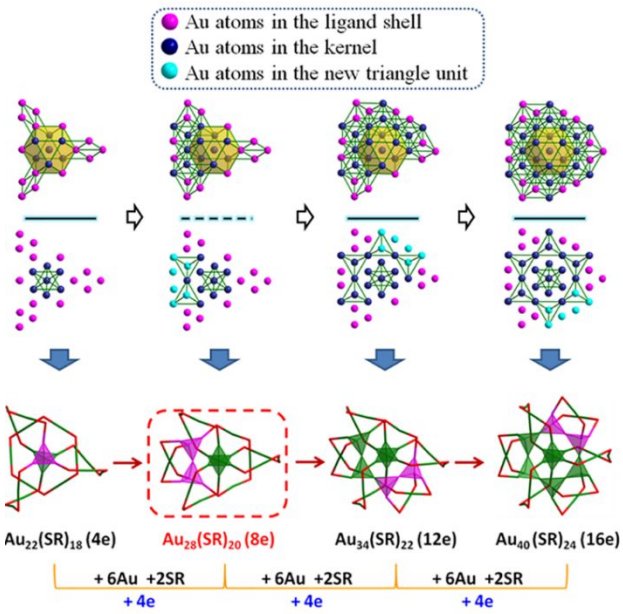

Figure 9. Gold atom framework evolution in the fcc gold nanoclusters. The SR groups in the fcc clusters are not displayed for clarity. The kernel and ligand-shell gold atoms are distinguished by different colors (pink balls, ligand-shell gold atoms; indigo balls, core gold atoms; turquoise balls, core gold atoms that increases or decreases in a sequence of clusters). Adapted with permission from ref 57, Copyright © 2018, American Chemical Society.

4. Fusion of fcc cubes

The face-centered cubic (fcc) unit cell comprises 8 vertices and 6 face centers and, hence, a total of 14 atoms in the unit. Zheng et al. reported a unique series of silver nanoclusters undergo 1-, 2- and 3-dimensional fusion of 14-atom fcc cubes to form super-rods (n), super-squares (n^2) and super-cubes (n^3).[61] Among them, $Ag_{14}(SPhF_2)_{12}(PPh_3)_8$ is the simplest fcc cube.[62,63] When fusing four of such simple Ag_{14} fcc cubes together via face sharing, a square like $Ag_{38}(SPhF_2)_{26}(P^nBu_3)_8]$ (2^2) metal framework was obtained as shown in Figure 10.[61] Further aggregation of another four Ag_{14} fcc cubes or one more square-like 2^2 gives rise to the cubic-structured $[Ag_{63}(SPhF_2)_{36}(P^nBu_3)_8]^+$ (2^3).[64] The missing, linearly assembled 2^1 Ag_{23} via fusion of two fcc cubes into a super-rod was later discovered by Li's group.[65] However, in Ag_{23} these two units twisted with respect to each other by ca. 27° along the longitudinal axis of the rod cluster. This leads to C_2 symmetry of the overall Ag framework, thus Ag_{23} has a chiral structure that originates from atomic arrangement of its metal core rather than configurations of the protecting ligands. Interestingly, the surface ligands share common binding features among the above 4 sizes in the series, i.e., the thiolate ligands cap the faces and edges of the cube (or half cube) while the phosphine ligands are terminally bonded to the cube's (or half-cube's) eight corners.

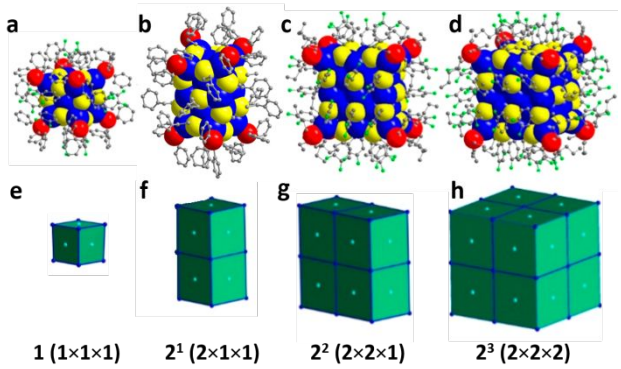

Figure 10. Crystal structures of Ag cubes: (a) $[Ag_{14}(SPhF_2)_{12}(PPh_3)_8]$ (1); (b) $[Ag_{23}(PPh_3)_8(SC_2H_4Ph)_{18}]$ (2^1) (c) $[Ag_{38}(SPhF_2)_{26}(PnBu_3)_8]$ (2^2); (c) $[Ag_{63}(SPhF_2)_{36}(PnBu_3)_8]^+$ (2^3) clusters, and their corresponding models (e–h) depicted as the idealized fcc close-packing growth sequence of the corresponding cubes. Color codes: blue and light blue sphere, Ag; red sphere, P; yellow sphere, S; green, F; gray, C. Adapted with the permission from refs 61 and 65, Copyright © 2017, American Chemical Society.

In this series, the evolution of electronic properties showed decreasing HOMO-LUMO gaps and the consequent red-shift of absorption peaks. Of note, Ag_{14} is a 2e superatom with HOMO-LUMO gap of 2.07 eV and the optical absorption shows peaks at 530 and 368 nm. The Ag_{23} shows a strong peak at 515 nm and a weak tail band over 600–700 nm, with the HOMO-LOMO gap being ca. 1.4 eV. More interestingly, it possesses an unpaired electron (the number of free valance electrons: 23–18 = 5e), evidenced by the electron paramagnetic resonance (EPR) signal.[61] For the larger ones, 2^2 and 2^3 have 12e and 26e, respectively, and HOMO-LUMO gaps were calculated to be 0.67 and 0.07 eV (in the cationic state), respectively.[64] UV–vis spectra of 2^2 and 2^3 in CH_2Cl_2 exhibit multi-band broad optical absorption: for 2^2, three peaks at 413, 507, 563 nm, and for 2^3, four peaks at 325, 415, 470, and 840 nm.[64]

Another series with fcc kernels pertains to the box-like Ag_{46}, Ag_{67} and Ag_{88} series (Figure 11).[66] Among them, the $[Ag_{67}(SPhMe_2)_{32}(PPh_3)_8]^{3+}$ was earlier experimentally reported by Alhilaly et al,[67] where the other two remain to be synthesized. Single crystal X-ray diffraction indicated that the Ag_{67} structure is composed of an Ag_{23} kernel protected by a layer of $Ag_{44}S_{32}P_8$ arranged in the shape of a box. Unlike the common Ag_{13} icosahedron geometry, the Ag_{23} kernel was formed through a cuboctahedron sharing opposite square faces with two Ag_8 crowns and then capped by two silver atoms at the open crown positions. This crowning of the Ag_{13} cuboctahedron leads to the box-shape growth of the Ag_{67} cluster. The entire cluster is stabilized by 8 AgS_3P motifs and 8 bridging thiolates.

Figure 11. Side views of the structures of $[Ag_{46}(SH)_{24}(PH_3)_8]^{2+}$ (left), $[Ag_{67}(SH)_{32}(PH_3)_8]^{3+}$ (middle), and $[Ag_{88}(SH)_{40}(PH_3)_8]^{2-}$ (right). The atoms within the dashed-frame indicate the $Ag_{21}(SH)_8$ block that is added or removed to/from the $[Ag_{67}(SH)_{32}(PH_3)_8]^{3+}$ model to build the fictive nanoclusters. Adapted with permission from ref 66, Copyright © 2017, American Chemical Society

Of note, after adding or removing a block of $Ag_{21}(SH)_8$ atoms to/from the $[Ag_{67}(SH)_{32}(PH_3)_8]^{3+}$ (simplified) model via calculations,

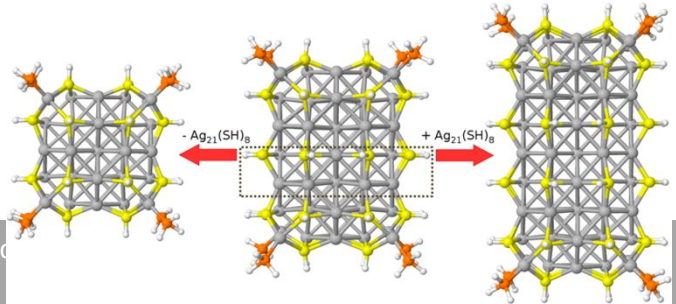

two box-like structures with equally good geometric stability and coordination as in the experimentally synthesized $[Ag_{67}(SPhMe_2)_{32}(PPh_3)_8]^{3+}$ nanocluster were predicted, with formulas of $[Ag_{46}(SH)_{24}(PH_3)_8]^{2+}$ and $[Ag_{88}(SH)_{40}(PH_3)_8]^{2-}$. Experimentally, $[Ag_{46}(SR)_{24}(PPh_3)_8]^{2+}$ (SR = 2,5-dimethylbenzenethiolate) has recently been synthesized and crystallized.[68,69] The structure was reported to be fcc, similar to the $[Ag_{46}(SH)_{24}(PH_3)_8]^{2+}$ model. Based on the electron counting, the number of valence electrons of Ag_{46} is 20, and 50 for Ag_{88}. Compared to the 0.36 eV HOMO–LUMO band gap of the experimentally known Ag_{67} nanocluster, the 1.0 eV gap for Ag_{46} and 0.46 eV for Ag_{88} may indicate even higher electronic stability.[66]

Conclusion

With the help of X-ray single crystal structure information and predictions through DFT calculations, several series of polyhedron-based fusion growth patterns have been revealed. Specifically, fusion growth based on the icosahedral Au_{13} and tetrahedral Au_4 as well as the fcc cube is summarized in this mini-Review. The specific modes include vertex- and face-sharing in a linear or cyclic manner, as well as stacking of 14-atom cubic units. As the size increases in each series, some general trends of the optical property evolution are found, such as the HOMO-LUMO gap shrinking and spectral redshifting. These series of nanoclusters offer valuable information on the size and structure evolution of coinage metal nanoclusters. More magic series and deeper understanding of size relationship of nanoclusters are to be explored in future work. The evolution patterns and geometry/electronic-structure correlations will shed light on the fusion growth mechanisms of nanostructures,[70] facilitate the investigation on the transition behaviour,[26] and open new opportunities by transforming the fundamental discoveries to practical applications.[71]

Conflicts of interest

There are no conflicts to declare.

Acknowledgements

R.J. acknowledges financial support from the National Science Foundation (DMR-1808675).

Notes and references

1 M. Zhou, T. Higaki, G. Hu, M. Y. Sfeir, Y. Chen, D. Jiang and R. Jin, *Science*, 2019, **364**, 279.
2 S. Hossain, Y. Niihori, L. V. Nair, B. Kumar, W. Kurashige and Y. Negish, *Acc. Chem. Res.*, 2018, **51**, 3114.
3 J. Liu, F. Alkan, Z. Wang, Z. Zhang, M. Kurmoo, Z. Yan, Q. Zhao, C. M. Aikens, C. Tung and D. Sun, *Angew. Chem. Int. Ed*., 2019, **58**, 195.
4 S. Zhang, F. Alkan, H. Su, C. M. Aikens, C. Tung and D. Sun, *J. Am. Chem. Soc.*, 2019, **141**, 4460.
5 S. Sharma, K. K. Chakrahari, J. Y. Saillard and C. Liu, *Acc. Chem. Res.*, 2018, **51**, 2475.
6 E. G. Mednikov and L. F. Dahl, *Phil. Trans. R. Soc. A* 2010, **368**, 1301.
7 N. Goswami, Q. Yao, T. Chen and J. Xie, *Coord. Chem. Rev.*, 2016, **329**, 1.
8 Z. Lei, X. Wan, S. Yuan, Z. Guan and Q. Wang, *Acc. Chem. Res.*, 2018, **51**, 2465.
9 Y. Li, J. Wang, P. Luo, X. Ma, X. Dong, Z. Wang, C. Du, S. Zang and T. C. W. Mak, *Adv. Sci.*, 2019, 1900833.
10 A. Ghosh, R. Huang, B. Alamer, E. A. Hamad, M. N. Hedhili, O. F. Mohammed and O. M. Bakr, *ACS Materials Lett.*, 2019, **1**, 297.
11 R. Jin, H. Qian, Z. Wu, Y. Zhu, M. Zhu, A. Mohanty and N. Garg, *J. Phys. Chem. Lett.,* 2010, **1**, 2903.
12 C. Zeng, Y. Chen, A. Das and R. Jin, *J. Phys. Chem. Lett.*, 2015, **6**, 2976.
13 C. Zeng, H. Qian, T. Li, G. Li, N. Rosi, B. Yoon, R. Barnett, R. Whetten, U. Landman and R. Jin, *Angew. Chem., Int. Ed*., 2012, **51**, 13114.
14 C. Liu, T. Li, G. Li, K. Nobusada, C. Zeng, G. Pang, N. Rosi and R. Jin, *Angew. Chem., Int. Ed.,* 2015, **54**, 9826.
15 S. Chen, S. Wang, J. Zhong, Y. Song, J. Zhang, H. Sheng, Y. Pei and M. Zhu, *Angew. Chem., Int. Ed.,* 2015, **54**, 3145.
16 T. Higaki, C. Liu, C. Zeng, R. Jin, Y. Chen, N. L. Rosi and R. Jin, *Angew. Chem., Int. Ed.,* 2016, **55**, 6694.
17 M. Zhu, C. Aikens, F. Hollander, G. Schatz and R. Jin, *J. Am. Chem. Soc.,* 2008, **130**, 5883.
18 C. Zeng, Y. Chen, K. Kirschbaum, K. Appavoo, M. Y. Sfeir and R. Jin, *Sci. Adv.* 2015, **1**, e1500045.
19 R. Jin, C. Zeng, M. Zhou and Y. Chen, *Chem. Rev.,* 2016, **116**, 10346.
20 I. Chakraborty and T. Pradeep, *Chem. Rev.*, 2017, **117**, 8208.
21 N. Yan, N. Xia, L. Liao, M. Zhu, F. Jin, R. Jin and Z. Wu, *Sci. Adv.* **2018**, *4*, eaat7259.
22 A. Das, T. Li, K. Nobusada, C. Zeng, N. Rosi and R. Jin, *J. Am. Chem. Soc.,* 2013, **135**, 18264.
23 Y. Song, S. Wang, J. Zhang, X. Kang, S. Chen, P. Li, H. Sheng, and M. Zhu, *J. Am. Chem. Soc.,* 2014, **136**, 2963.
24 C. Zeng, Y. Chen, K. Kirschbaum, K. J. Lambright and R. Jin, *Science* 2016, **354**, 1580.
25 B. Teo, M. Hong, H. Zhang and D. Huang, *Angew. Chem., Int. Ed.,* 1987, **26**, 897.
26 T. Higaki, M. Zhou, K. Lambright, K. Kirschbaum, M. Y. Sfeir and R. Jin, *J. Am. Chem. Soc.* **2018**, *140*, 5691.
27 R. Jin, *Nanoscale,* 2010, **2**, 343.
28 Y. Shichibu and K. Konishi, *Small,* 2010, **6**, 1216.
29 Y. Shichibu, Y. Negishi, T. Watanabe, N. Chaki, H. Kawaguchi and T. Tsukuda, *J. Phys. Chem. C*, 2007, **111**, 7845.
30 H. Qian, W. Eckenhoff, M. Bier, T. Pintauer and R. Jin, *Inorg. Chem*., 2011, **50**, 10735.
31 R. Jin, C. Liu, S. Zhao, A. Das, H. Xing, C. Gayathri, Y. Xing, N. Rosi, R. Gil and R. Jin, *ACS Nano*., 2015, **8**, 8530.
32 K. Nobusada and T. Iwasa, *J. Phys. Chem. C,* 2007, **111**, 14279.
33 M. Zhou, R. Jin, M. Y. Sfeir, Y. Chen, Y. Song and R. Jin, *Proc. Natl. Acad. Sci. USA.*, 2017, **114**, E4697.
34 B. K. Boon, and K. Kelly, *J. Am. Chem. Soc.,* 1984, **106**, 2224.
35 S. Yang, J. Chai, T. Chen, B. Rao, Y. Pan, H. Yu and M. Zhu. *Inorg. Chem.,* 2017, **56**, 1771.
36 S. Wang, X. Meng, A. Das, T. Li, Y. Song, T. Cao, X. Zhu, M. Zhu and R. Jin, *Angew. Chem. Int. Ed.,* 2014, **53**, 2376.
37 T. Iwasa, K. Nobusada and A. Nakajima, *J. Phys. Chem. C* 2013, **117**, 24586.
38 B. K. Teo, H. Zhang and X. Shi, *J. Am. Chem. Soc.,* 1990, **112**, 8552.
39 Y. Song, F. Fu, J. Zhang, J. Chai, X. Kang, P. Li, S. Li, H. Zhou and M. Zhu, *Angew. Chem. Int. Ed*., 2015, **54**, 8430.
40 H. Qian, W. Eckenhoff, Y. Zhu, T. Pintauer and R. Jin, *J. Am. Chem. Soc.*, 2010, **132**, 8280.

41 T. Dainese, S. Antonello, S. Bogialli, W. Fei, A. Venzo and F. Maran, *ACS Nano*, 2018, **12**, 7057.
42 S. Malola, L. Lehtovaara and H. Häkkinen, *J. Phys. Chem. Lett.,* 2014, **5**, 1329.
43 S. Malola, L. Lehtovaara, S. Knoppe, K. Hu, R. Palmer, T. Bürgi and H. Häkkinen, *J. Am. Chem. Soc.*, 2012, **134**, 19560.
44 H. Tsunoyama, Y. Negishi and T. Tsukuda, *J. Am. Chem. Soc.* 2006, **128**, 6036.
45 H. Tsunoyama, P. Nickut, Y. Negishi, K. Al-Shamery, Y. Matsumoto and T. Tsukuda, *J. Phys. Chem. C*, 2007, **111**, 4153.
46 R. Tsunoyama, H. Tsunoyama, P. Pannopard, J. Limtrakul and T. Tsukuda, *J. Phys. Chem. C*, 2010, **114**, 16004.
47 C. Zeng, Y. Chen, K. Iida, K. Nobusada, K. Kirschbaum, K. Lambright and R. Jin, *J. Am. Chem. Soc.*, 2016, **138**, 3950.
48 C. Zeng, C. Liu, Y. Chen, N. Rosi and R. Jin, R., *J. Am. Chem. Soc.*, 2014, **136**, 11922.
49 C. Zeng, T. Li, A. Das, N. Rosi, and R. Jin, *J. Am. Chem. Soc.*, 2013, **135**, 10011.
50 C. Zeng, Y. Chen, C. Liu, K. Nobusada, N. Rosi and R. Jin, *Sci. Adv.,* 2015, **1**, e1500425.
51 Z. Ma, P. Wang and Y. Pei, *Nanoscale*, 2016, **8**, 17044.
52 Y. Pei, P. Wang, Z. Ma and L. Xiong, *Acc. Chem. Res.,* 2019, **52**, 23.
53 W. Xu, Y. Li, Y. Gao and X. Zeng, *Nanoscale*, 2016, **8**, 7396.
54 Z. Ma, P. Wang, G. Zhou, J. Tang, H. Li and Y. Pei, *J. Phys. Chem. C*, 2016, **120**, 13739.
55 Y. Chen, C. Liu, Q. Tang, C. Zeng, T. Higaki, A. Das, D. Jiang, N. Rosi and R. Jin, *J. Am. Chem. Soc.*, 2016, **138**, 1482.
56 H. Dong, L. Liao, S. Zhuang, C. Yao, J. Chen, S. Tian, M. Zhu, X. Liu, L. Li, and Z. Wu, *Nanoscale*, 2017, **9**, 3742.
57 L. Xiong, S. Yang, X. Sun, J. Chai, B. Rao, L. Yi, M. Zhu and Y. Pei, *J. Phys. Chem. C,* 2018, **122**, 14898.
58 Y. Pei, J. Tang, X. Tang, Y. Huang and X. Zeng, *J. Phys. Chem. Lett*., 2015, **6**, 1390.
59 X. Sun, P. Wang, L. Xiong, Y. Pei, *Chem. Phys. Lett.*, 2018, **704**, 68.
60 C. Zeng, Y. Chen, C. Liu, K. Nobusada, N. Rosi and R. Jin, *Sci. Adv*., 2015, **1**, e1500425.
61 B. K. Teo, H. Yang, J. Yan and N. Zheng, *Inorg. Chem.*, 2017, **56**, 11470.
62 H. Yang, J. Lei, B. Wu, Y. Wang, M. Zhou, A. Xia, L. Zheng and N. Zheng, *Chem. Commun.*, 2013, **49**, 300-302.
63 L. Gell, L. Lehtovaara and H. Häkkinen, *J. Phys. Chem. A*, 2014, **118**, 8351.
64 H. Yang, J. Yan, Y. Wang, H. Su, L. Gell, X. Zhao, C. Xu, B. K. Teo, H. Häkkinen and N. Zheng, *J. Am. Chem. Soc*., 2017, **139**, 31.
65 C. Liu, T. Li, H. Abroshan, Z. Li, C. Zhang, H. Kim, G. Li and R. Jin. *Nat. Commun.*, 2018, **9**, 744.
66 R. Mosqueda, S. Kaappa, S. Malola and H. Häkkinen, *J. Phys. Chem. C*, 2017, **121**, 10698.
67 M. Alhilaly, M. Bootharaju, C. Joshi, T. Besong, A. Emwas, R. Juarez-Mosqueda, S. Kaappa, S. Malola, K. Adil, A. Shkurenko, H. Häkkinen, M. Eddaoudi and O. Bakr, *J. Am. Chem. Soc.,* 2016, **138**, 14727.
68 J. Chai, S. Yang, Y. Lv, T. Chen, S. Wang, H. Yu and M. Zhu, *J. Am. Chem. Soc.*, 2018, **140**, 15582-15585.
69 M. Bodiuzzaman, A. Ghosh, K. S. Sugi, A. Nag, E. Khatun, B. Varghese, G. Paramasivam, S. Antharjanam, G. Natarajan and T. Pradeep, *Angew. Chem. Int. Ed.* 2019, **58**, 189.
70 R. Jin, Y. C. Cao, E. Hao, G. S. Métraux, G. C. Schatz and C. A. Mirkin, *Nature* 2003, **425**, 487.
71 T. Higaki, Q. Li, M. Zhou, S. Zhao, Y. Li, S. Li and R. Jin, *Acc. Chem. Res.* 2018, **51**, 2764.

Graphic Abstract:

This mini-Review summarizes the fusion growth patterns of metal nanoclusters based upon M_4, M_{13} and M_{14} building blocks.